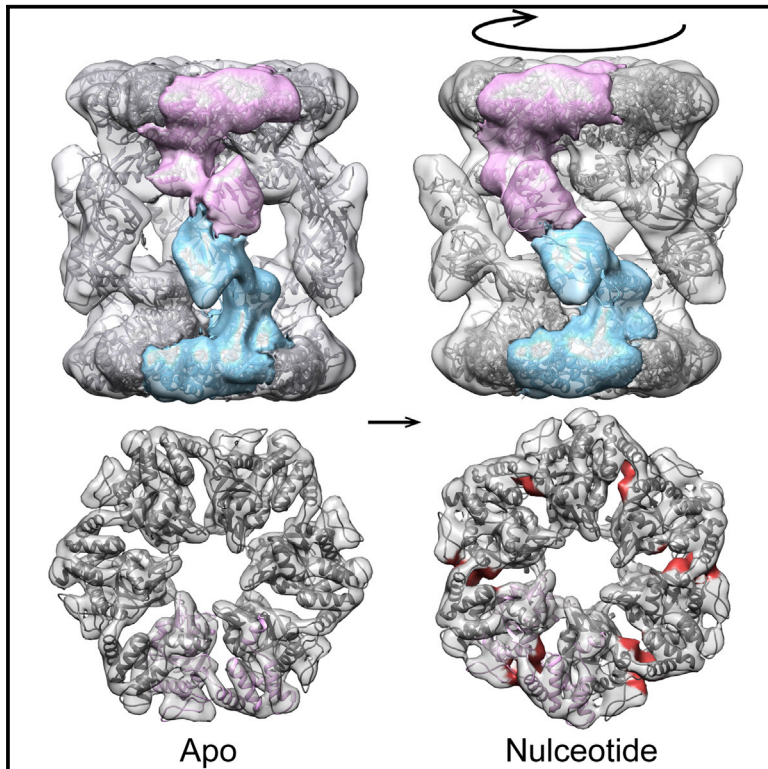# Architecture and Nucleotide-Dependent Conformational Changes of the Rvb1-Rvb2 AAA+ Complex Revealed by Cryoelectron Microscopy

Graphical Abstract

Apo   Nulceotide

Authors

Caroline A. Ewens, Min Su, Liang Zhao, Nardin Nano, Walid A. Houry, Daniel R. Southworth

Correspondence

dsouth@umich.edu

In Brief

Rvb1/2 is an essential ATP-dependent machine required for the assembly and function of large macromolecular complexes. Ewens et al. describe dynamical structures of the Rvb1/2 complex by cryoelectron microscopy and identify nucleotide-dependent conformations that could power its mechanical chaperone activity.

Highlights

- Cryo-EM reveals the architecture and nucleotide states of the Rvb1/2 AAA+ complex

- The dodecamer arrangement and insertion domains rotate in response to nucleotide

- Symmetric/asymmetric populations involving insertion-domain variability are defined

- Conformational changes reveal insight into mechanically driven remodeling functions

CrossMark

CellPress

CellPress

Architecture and Nucleotide-Dependent Conformational Changes of the Rvb1-Rvb2 AAA+ Complex Revealed by Cryoelectron Microscopy

Caroline A. Ewens,[1] Min Su,[1] Liang Zhao,[2] Nardin Nano,[2] Walid A. Houry,[2] and Daniel R. Southworth[1,*]
[1]Department of Biological Chemistry, Life Sciences Institute, University of Michigan, Ann Arbor, MI 48109, USA
[2]Department of Biochemistry, University of Toronto, Toronto, ON M5S 1A8, Canada
*Correspondence: dsouth@umich.edu
http://dx.doi.org/10.1016/j.str.2016.03.018

SUMMARY

Rvb1 and Rvb2 are essential AAA+ proteins that interact together during the assembly and activity of diverse macromolecules including chromatin remodelers INO80 and SWR-C, and ribonucleoprotein complexes including telomerase and snoRNPs. ATP hydrolysis by Rvb1/2 is required for function; however, the mechanism that drives substrate remodeling is unknown. Here we determined the architecture of the yeast Rvb1/2 dodecamer using cryoelectron microscopy and identify that the substrate-binding insertion domain undergoes conformational changes in response to nucleotide state. 2D and 3D classification defines the dodecamer flexibility, revealing distinct arrangements and the hexamer-hexamer interaction interface. Reconstructions of the apo, ATP, and ADP states identify that Rvb1/2 undergoes substantial conformational changes that include a twist in the insertion-domain position and a corresponding rotation of the AAA+ ring. These results reveal how the ATP hydrolysis cycle of the AAA+ domains directs insertion-domain movements that could provide mechanical force during remodeling or helicase activities.

INTRODUCTION

Rvb1 and Rvb2 are highly conserved, essential eukaryotic members of the AAA+ (ATPases associated with various cellular activities) helicase family related to bacterial RuvB (Kanemaki et al., 1999). They function together as the Rvb1/2 complex in numerous cellular pathways including chromatin remodeling (Shen et al., 2000), phosphatidylinositol 3-kinase-related protein kinase (PIKK) signaling (Izumi et al., 2010), telomerase assembly (Venteicher et al., 2008), and box C/D small nucleolar ribonucleoprotein (snoRNP) biogenesis (McKeegan et al., 2009). Rvb1/2 is proposed to function as a chaperone-like machine by directing the assembly, stability, and activity of the large protein and nucleoprotein complexes involved in these various pathways (Nano and Houry, 2013; Neuwald et al., 1999; Zaarur et al., 2015). The Rvb1/2 complex is a key component of the INO80 and SWR-C

(Swi/Snf2-related) chromatin remodeling complexes (Gerhold and Gasser, 2014), recruiting the Arp5-Ies6 module in INO80 that is involved in nucleosome sliding (Jónsson et al., 2004; Yao et al., 2015) and interacting with the ATPase domain of Swr1 in the SWR-C complex (Wu et al., 2005). During box C/D snoRNP assembly Rvb1/2 is required as part of the conserved R2TP (Rvb1-Rvb2-Tah1-Pih1) complex that binds the Hsp90 molecular chaperone and core proteins 15.5K, Nop56, and Nop58 in an ATP-dependent manner (McKeegan et al., 2009; Zhao et al., 2005). While ATP hydrolysis by Rvb1 and Rvb2 is essential in vivo (Jónsson et al., 2001) and required for helicase activity (Gribun et al., 2008), the precise catalytic function of Rvb1/2 in these diverse assemblies is not fully understood.

The conserved AAA+ domains in Rvb1 and Rvb2 are made up of large and small subdomains that include Walker A and B motifs, nucleotide sensor sequences, and an arginine finger motif, which are necessary for ATP binding and hydrolysis (Nano and Houry, 2013). Crystal structures of human (Gorynia et al., 2011) and thermophilic yeast (Chaetomium thermophilum) (Lakomek et al., 2015; Silva-Martin et al., 2016) Rvb1/2 confirm the alternating subunit arrangement and a hexamer ring structure that is composed of the AAA+ domains, similar to other homologous complexes (Tucker and Sallai, 2007). The nucleotide-binding pocket is positioned near the subunit interface with the arginine finger of the adjacent protomer interacting in the pocket to coordinate hydrolysis. A large, 18-kDa, insertion domain (I domain) that is unique to the Rvb proteins separates the Walker A and B sequences and forms a distinct L-shaped structure that extends away from the AAA+ hexamer ring (Lakomek et al., 2015; Matias et al., 2006). This domain is composed of an α-helical base and a globular α/β tip that are connected by two flexible β strands. The tip region of the I domain is structurally similar to the single-stranded binding domain of replication factor A and has been shown to bind DNA and RNA in solution, supporting a direct role in helicase functions (Matias et al., 2006).

The Rvb1/2 complex exists in hexameric and dodecameric (double hexamer) forms (Jeganathan et al., 2015), likely reflecting its large functional diversity; however, the specific roles of these two states are unknown. ATP hydrolysis is required for Rvb1/2 function (Jónsson et al., 2001) and both the hexamer and dodecamer forms are active (Gribun et al., 2008; Torreira et al., 2008). Furthermore, these complexes have recently been identified in structural models of the SWR1 and INO80 complexes (Nguyen et al., 2013; Tosi et al., 2013; Watanabe et al., 2015), supporting functions in chromatin remodeling. I-domain
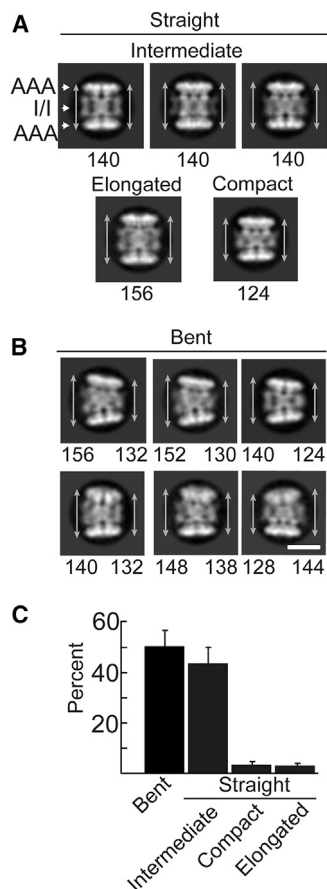
CrossMark

Figure 1. The Rvb1/2 Dodecamer Adopts Distinct Straight and Bent Hexamer-Hexamer Arrangements

(A) 2D reference-free classification of the apo Rvb1/2 dodecamer by cryo-EM identifies averages with straight dodecamer side views showing two parallel AAA+ rings connected by symmetric I-domain density (I/I) with "Intermediate," "Elongated," and "Compact" lengths. Measurements are indicated by arrows and listed below each average in angstroms.

(B) Averages from the same classification reveal "Bent" dodecamers with non-parallel, tilted AAA+ rings resulting in different lengths on either side of the dodecamer. Measurements are indicated by arrows and listed below each average in angstroms. Scale bar, 50 Å.

(C) Histogram showing the percentage of the dodecamer side-view particles in the different conformations. The error bars represent the SD from three separate datasets.

interactions join the two hexamer rings together to form the dodecamer (Cheung et al., 2010; Torreira et al., 2008), but their flexibility has limited electron microscopy (EM) structural characterization and full-length crystal structures have identified several conformations (Lakomek et al., 2015; Matias et al., 2006). Thus, the overall architecture of the Rvb1/2 complex and conformational state of I domains remains a significant question. In addition, while nucleotide-dependent conformational changes in the AAA+ ring have been proposed by 2D negative-stain EM (Gribun et al., 2008), it is unknown whether larger domain rearrangements, such as movement of the I domains, occur during ATP hydrolysis.

Here we use cryo-EM to characterize the solution structure of the yeast (*Saccharomyces cerevisiae*) Rvb1/2 dodecamer in

different nucleotide states. Using extensive 2D and 3D cryo-EM classification analysis, we are able to sort the conformational heterogeneity and identify distinct forms of the dodecamer resulting from flexible I-domain interactions that stabilize parallel, "straight" and non-parallel, "bent" arrangements of the AAA+ rings. We determined a 3D reconstruction and molecular model of apo Rvb1/2 from the predominant homogeneous class that reveals the I-domain conformation and interaction interface that connects the two hexamer rings together. Mutation of residues identified to be at the hexamer-hexamer interface abolishes the dodecamer, thereby confirming the proposed I-domain arrangement and their function in dodecamer stability. Reconstructions of the ATP and ADP states along with higher-resolution refinements of the AAA+ hexamer rings reveal nucleotide-specific conformational changes that include a stepwise rotation of the AAA+ ring and corresponding rotation of I domains around the dodecamer. This work supports a model whereby the ATP hydrolysis cycle drives large conformational rearrangements in the I-domain position that could regulate interactions during the assembly of ribonucleoprotein complexes and provide mechanical force during helicase and remodeling cycles.

RESULTS

I-Domain Conformations Stabilize Distinct Bent and Straight Forms of the Rvb1/2 Dodecamer

Previous studies identified that the Rvb1/2 dodecamer is variable and exists in multiple conformations (Jeganathan et al., 2015; López-Perrote et al., 2012; Matias et al., 2006). To further characterize the nature of this variability and determine the architecture of Rvb1/2 complex, we enriched the dodecamer form by separation from the hexamer and subjected it to single-particle EM studies. Initial EM analysis confirmed that the vast majority of particles are dodecameric, with side views showing two dense layers at the top and bottom of the particle that corresponded to two AAA+ rings (Figure S1A). We next collected cryo-EM datasets and performed 2D and 3D classification analysis of the Rvb1/2 dodecamer in the apo state. 2D classification identified multiple conformations and orientations, including some top-down views with six-fold symmetry and distinct structural features of the AAA+ domains (Figures S1B and S1C). Side views of the dodecamer were predominant, showing clear density for the two AAA+ rings and I domains in between. Re-projections of the dodecamer crystal structure (Lakomek et al., 2015) show a non-uniform I-domain arrangement that does not match the class averages, as judged by visual comparison, indicating that this conformation is not detectable in the data (Figure S1D). Furthermore, this conformation was also not observed following a 3D classification using the crystal structure as a starting model (Figure S1E) or in any subsequent classification analysis, but nevertheless may be present in a small subpopulation that was not resolvable.

To characterize the conformational variability and identify homogeneous subpopulations, we pooled and further classified particles from the well-defined side-view classes. From these averages we identified distinct conformational states of the dodecamer defined as straight and bent arrangements based on the respective parallel or non-parallel positions of the AAA+ rings (Figures 1A and 1B). The lengths were measured on either side of

each projection average to determine the fraction of particles in the different conformations (Figure 1C). The class averages of the straight conformations showed defined AAA+ ring layers and distinct, symmetric stripes of density between the rings that are attributable to the I domains interacting across and connecting the two rings together (Figure 1A). The majority of these averages, 44% of the side-view particles, are intermediate in length, measuring approximately 140 Å. Minor populations (3%) of a compact form (124 Å) and an elongated form (156 Å) are also identified. These sizes are consistent with previously reported forms of the dodecamer (Jeganathan et al., 2015; López-Perrote et al., 2012). A significant dodecamer population (50% of side views) is in a bent arrangement, where the length between the AAA+ rings varies across the particle (Figure 1B). Well-defined stripes of density for the I domains are apparent, indicating that these averages represent distinct conformations. The maximum and minimum lengths, 156 and 124 Å, match the small population of compact and elongated straight dodecamers. However, a wide range of asymmetry is present, indicating that the dodecamer can exist with varied degrees of bending. Bent particles are also observed in negative-stain images, indicating that this was not the result of the cryo-grid preparation (Figure S1A).

To further analyze the architecture of the bent conformations, we performed a 3D classification and refinement with no imposed symmetry. Two predominant 3D classes identify bent conformations with the AAA+ rings tilted by 5° in one model and 12° in the other (Figure S1F). The AAA+ rings retain six-fold symmetry and match crystal structures. Density corresponding to the I domains connects hexamers together in varied arrangements and appears to undergo a large contraction and expansion around the complex that results in the bent, non-parallel arrangement of the AAA+ rings. Overall our classification analysis resolves the conformational flexibility of Rvb1/2, identifying distinct asymmetric states of the dodecamer that arise from varied I-domain conformations around the complex, which stabilize different relative orientations of the AAA+ rings. Furthermore, with this classification we were able to identify a significant population of well-defined symmetric dodecamers with parallel AAA+ rings that are amenable to higher-resolution 3D reconstruction and analysis.

3D Reconstruction of the Apo Rvb1/2 Dodecamer in the Straight Conformation Reveals the I-Domain Organization and Hexamer-Hexamer Interactions

Previous EM structural analysis of Rvb1/2 has been limited by the flexibility of the complex, while multiple conformational arrangements of the I domains have been observed in crystal structures; thus the architecture of the dodecamer and conformation in solution remains a question. From our 2D classification we identified that a substantial number of apo Rvb1/2 dodecamer particles appear similar in length with a symmetric arrangement of the I domains and parallel orientation of the AAA+ rings (Figure 1A). Single particles from these averages (approximately 130,000) were combined for additional 3D classification and refinement (Figure S2A). Two classes (classes 1 and 3) were identified to be similar in length and showed clear definition of the I domains. Class 2 was poorly defined and not characterized further, while class 4 showed well-defined I domains but was in an elongated conformation (~154 Å) compared with classes 1

and 3 (~140 Å). Additional 2D classification identified that class 4 contained a substantial proportion of bent, asymmetric particles (Figure S2B). Given this variability, data from class 4 were not used in subsequent refinements. In contrast, classes 1 and 3 were predominantly straight, with consistent dimensions and in good agreement with the models, so these classes were combined for further 3D refinement.

The final map was refined with D3 symmetry imposed, given the known alternating arrangement of the protomers (Gorynia et al., 2011; Lakomek et al., 2015), and showed an indicated resolution of 8.3 Å at Fourier shell correlation (FSC) = 0.143 and 9.4 Å at FSC = 0.5 (Figure S2C). The angular distribution for the particles included in the apo dodecamer reconstruction shows preferred side-view and top-view orientations along with additional views (Figure S2D). The reconstruction identifies Rvb1/2 in a double-ring dodecamer arrangement with planar hexameric AAA+ rings at the top and bottom, and L-shaped I-domain densities that protrude outward from each ring and connect the hexamers together (Figure 2A). The I-domain interactions form six elongated globular lobes that are tilted by approximately 15° from the three-fold axis in an evenly spaced arrangement around the middle of the dodecamer, equidistant from the AAA+ rings. At a higher density threshold the AAA+ rings remain visible and show higher-resolution features, indicating that these domains are more stable compared with the I domains (Figure 2B). Furthermore, local resolution calculations indicate that the resolution of the I-domain lobes is substantially lower than for the AAA+ rings (Figure S2E). Thus, some additional conformational variability of the I domains remaining in the data likely imposes limitations. Importantly, the symmetric arrangement of the I domains is consistent with our 2D analysis and re-projections of the final model match reference-free class averages, showing identical stripes of I-domain density (Figure S2F), supporting the dodecamer architecture identified in the reconstruction.

Structures of the AAA+ domains fit in the cryo-EM density extremely well (Figure 2C) and minor differences for each protomer are observed; however, the resolution is not sufficient for unambiguous assignment. When modeling is performed with intact monomer structures the I-domain globular tips do not match the cryo-EM density (Figure S2G). For Rvb1 in the *C. thermophilum* structure (Lakomek et al., 2015), the I domains are extended and nearly perpendicular to the AAA+ ring and the globular tip sits outside the cryo-EM density. The arrangement of Rvb2 in this structure as well as Rvb1 from the structure of the human ortholog (RuvBL1) (Matias et al., 2006) shows an improved fit; however, the globular tip also does not match the cryo-EM density due to the angle of the connecting β strands. Thus, the I domains in our reconstruction of the dodecamer are in different conformation with respect to the AAA+ ring. To achieve a more accurate model, we docked the I-domain base region and the tip (Figure S2H) as two separate rigid bodies to allow movement of their relative orientations. The final model (Figure 2C) shows a substantially improved fit for the I domains, with a cross-correlation of 0.93 calculated for the complete model. The I-domain fitting defines a hexamer-hexamer interaction interface in which the β8 strands of both subunits (Rvb1 175–181; Rvb2 165–171) are adjacent, potentially making direct contacts to stabilize the dodecamer (Figure 2D). In addition, the β6-β7 loops in Rvb1
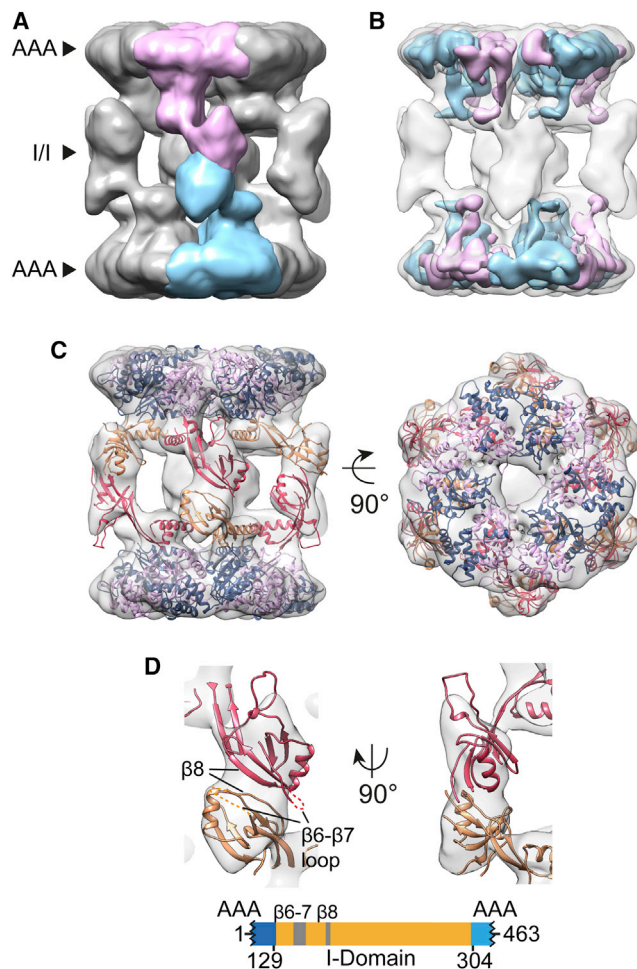
Figure 2. Cryo-EM Model Identifies I-Domain Conformation and Hexamer-Hexamer Interactions of the Rvb1/2 Dodecamer

(A) The final cryo-EM map of the apo Rvb1/2 dodecamer segmented to indicate Rvb1 (pink) and Rvb2 (blue) protomers, and showing density for two AAA+ rings (AAA) and the I-domain/I-domain (I/I) interactions.

(B) Map at a higher contour level showing features of the AAA+ domains and loss of density for the flexible I domains.

(C) Crystal structures (PDB: 4WVY) docked into the reconstruction showing the AAA+ domains (pink for Rvb1 and blue for Rvb2) and I domains (red for Rvb1 and orange for Rvb2).

(D) An enlarged view of the I-domain/I-domain region showing the molecular model and interaction interface involving β8 strands (residues 175–181 n Rvb1) and β6-β7 loop (residues 150–165 in Rvb1). A schematic below shows approximate locations (Rvb1 numbering) of I-domain tip regions (orange).

and Rvb2 (Rvb1 150–165; Rvb2 146–157) are nearby based on this fitting and may also play a role. These residues are not resolved in the crystal structure and are observed as a flexible loop in a nuclear magnetic resonance structure of human Rvb2 (PDB: 2CQA). Additional regions of the I-domain base (Rvb1 250–274, Rvb2 249–269) are not observed in our map, likely due to the flexibility. These residues are hypothesized to be involved in stabilizing the dodecamer (Gorynia et al., 2011) and could potentially be contributing to the globular density in the center of the reconstruction based on the connecting density in the I-domain base. Importantly, the I-domain arrangement we have

identified here orientates the putative DNA/RNA-binding interface in the I-domain tip (Matias et al., 2006) toward the outside of the dodecamer, making it accessible for interaction with potential substrates. Overall, the molecular model of apo Rvb1/2 reveals a distinct conformation of the I domains where the globular α/β tip is positioned to make substantial interactions across the hexamer-hexamer interface, potentially via the β8 strands, to stabilize the symmetric arrangement of the dodecamer.

Mutagenesis at the Predicted I-Domain Interface Destabilizes the Dodecamer

Our molecular model identifies a novel interaction interface between the hexamers involving the β8 strand and β6-β7 loop regions in the globular tip of the I domain (Figure 2D). To confirm this finding, we generated single point mutations in Rvb1 and Rvb2 to destabilize the dodecamer form and increase the number of hexamers (Figure 3A). Size-exclusion chromatography was used to assess the amount of dodecamer versus hexamer based on the relative proportions of the two peaks, which were defined by comparison with the known elution volumes for the wild-type hexamer (12.8 ml) and dodecamer (14.1 ml) (Figures 3B and 3C). Mutations that reverse charged residues in the β8 strands (R180E in Rvb1 and E166K in Rvb2) were chosen, and co-expressed and purified with the respective wild-type protomer. For both mutants the peak corresponding to the dodecamer was substantially reduced while the peak for hexamer complex increased, demonstrating that these mutations indeed destabilize dodecamer formation. A reduced ratio of dodecamers to hexamers was observed compared with wild-type by negative-stain EM analysis, but no overall structural differences in the dodecamer particles are seen (Figure S3A), indicating that the mutant complex remains properly folded. The Rvb1 mutation K161E, which is located in the β6-β7 loop, also showed a reduced dodecamer peak, supporting a role for the loop in stabilizing the dodecamer interaction. Both Rvb1 E146R and E150K mutations, located adjacent the proposed interface and predicted to not affect the interaction based on our model, showed no substantial change in the amount of dodecamer (Figure 3A). Based on these results, residues in the β8 strand and β6-β7 loop may be involved in salt-bridge interactions across the interface. However, we were unable to identify specific sites due to the lower resolution of the cryo-EM map in this region. These mutant complexes showed identical behavior following incubations with ADP, indicating that the presence of nucleotide does not alter dodecamer stability (Figure S3B). Purified dodecamer and hexamer as well as the R180E mutant complex were active for ATP hydrolysis with rates ($\sim$1.4 pmol ATP pmol Rvb^{-1} min^{-1}) equivalent to previously reported values (Gribun et al., 2008), indicating that ATP hydrolysis is independent of the dodecamer stability (Figure S3C). These results provide validation of the I-domain conformation and interaction surface proposed from our cryo-EM model and identify regions in the β8 strands and nearby loop in the I domain that likely stabilize the dodecamer via electrostatic interactions.

Reconstructions of ATP and ADP States Reveal Nucleotide-Specific Conformational Changes in the Rvb1/2 Dodecamer

ATP hydrolysis by Rvb1/2 is essential for yeast viability (Jónsson et al., 2001) and is thought to be required for specific
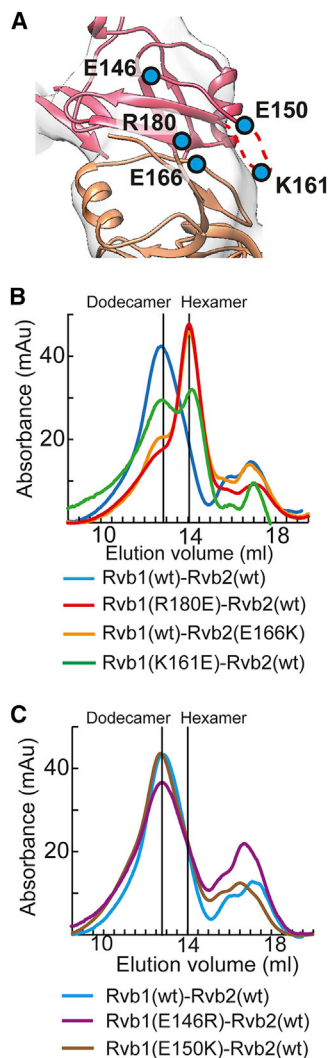
Figure 3. Mutational Analysis Identifies I-Domain Residues Involved in Rvb1/2 Dodecamer Stability

(A) Location of interface mutants based on the cryo-EM model of the dodecamer is shown (blue dots) in the I-domain globular tip of Rvb1 (red) and Rvb2 (orange). The dashed line represents the β6-β7 loop.

(B and C) Size-exclusion chromatography analysis of the dodecamer stability (elution volume versus absorbance at 280 nm) for wild-type Rvb1/2 (blue) compared with (B) Rvb1(R180E)-Rvb2(wt) (red), Rvb1(wt)-Rvb2(E166K) (orange), and Rvb1(K161E)-Rvb2(wt) (green) or (C) Rvb1(E146R)-Rvb2(wt) (purple) and Rvb1(E150K)-Rvb2(wt) (brown). The peaks corresponding to dodecamer and hexamer states eluted at 12.8 ml and 14.1 ml, respectively.

chaperone-like and helicase functions (Jónsson et al., 2004; Matias et al., 2015). However, conformational changes during the hydrolysis cycle that could drive mechanical remodeling functions are unknown. To investigate potential nucleotide-dependent changes in the Rvb1/2 complex, we collected cryo-EM datasets of the dodecamer following incubations with either AMPPNP (non-hydrolyzable ATP analog) to mimic the ATP state, or ADP. By 2D reference-free classification both datasets show equivalent proportions of straight and bent dodecamers as the apo-state data, indicating that the configuration of the AAA+ rings is not altered by the presence of nucleotide (Figure S4A

and S4B). For the apo data, the single particles in the 2D classes identified to be in a straight arrangement with parallel AAA+ rings were pooled for 3D classification and refinement (Figure S4C and S4D). The ATP- and ADP-state Rvb1/2 datasets were each separated into four 3D classes and in both cases one well-populated class was identified to be in a different conformation, with distinct I-domain arrangements, compared with apo Rvb1/2. The remaining classes were either poorly resolved or displayed I-domain positions similar to the apo-state arrangement. These nucleotide-specific classes, representing a substantial proportion of the data (29% and 30%, respectively), were further refined, and the resulting final maps show a resolution of 9.5 Å (11.6 Å at FSC = 0.5) for the ATP state and 7.8 Å (9.8 Å at FSC = 0.5) for the ADP state (Figure S2C). When the apo reconstruction was used as a starting model the refinement for both the ATP and ADP states converged to the respective conformations, establishing that these conformations are indeed representative of the data (Figures S4E and S4F). To determine whether the apo data contain a subset of particles similar to the ADP or ATP conformation, we implemented a 3D classification using the ADP-state map as a starting model (Figure S4G). None of final classes retained the ADP-state I-domain arrangement and, in general, converged to the apo conformation, indicating that the conformation is not detectable and thus requires nucleotide.

Rvb1/2 crystal structure monomers (PDB: 4WVY) were docked into the maps for the ATP and ADP states in the same manner as for the apo reconstruction, with the AAA+ domain and the I-domain base and tip regions treated as three separate rigid bodies. The docked models had correlation coefficients of 0.95 and 0.93 for the ATP- and ADP-state reconstructions, respectively. The correct hand of the maps was determined based on the fit of the crystal structure to the AAA+ domains and I-domain base that contain higher-resolution features in the cryo-EM map. Furthermore, higher-resolution refinements of the AAA+ ring unambiguously establish the correct hand of the maps (see below). Both the reconstructions and fitted models show a similar length (140 Å), and arrangement of the AAA+ rings and I-domain bases as the apo complex (Figures 4A and 4B). Overall these models identify a substantial conformational change in the orientation of the I-domain density across the hexamer/hexamer interface. By further comparison of the models, the positions of the I-domain globular tips are identified to be rotated clockwise from the top orientation about the six-fold axis by 23° and 30° for the ATP and ADP states, respectively, compared with the apo-state position (Figure 4C and Movie S1). Furthermore, the relative position of AAA+ rings shifts correspondingly, with one ring rotating with respect to the second ring by 29° in the ATP state and 32° in the ADP state (Figure 4D). Based on the fit of the I-domain tips, the same hexamer-hexamer interaction interface appears to be maintained in the three conformational states. This is further supported by our dodecamer stability analysis of the I-domain mutant complexes in the presence of ADP (Figure S3B). The largest conformational changes occur between the apo and ADP states while the ATP state appears intermediate and similar to the ADP-bound form, indicating that the changes are on path with respect to nucleotide binding and hydrolysis. These results reveal that the Rvb1/2 dodecamer undergoes substantial, nucleotide-specific
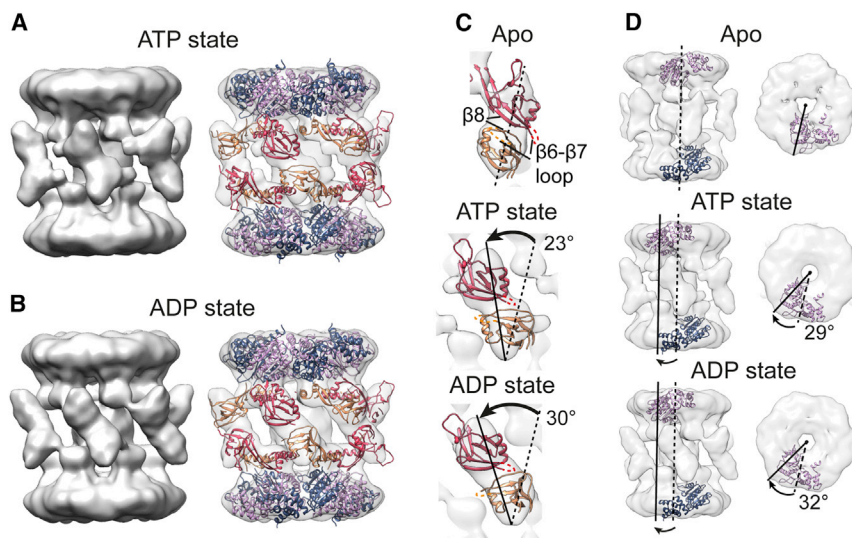
Figure 4. Nucleotide-Specific Conformational Changes Identified in Cryo-EM Reconstructions of Rvb1/2 in the ATP and ADP States

(A and B) The cryo-EM reconstructions and pseudo-atomic models (PDB: 4WVY) of the Rvb1/2 dodecamer incubated with (A) AMPPNP (non-hydrolyzable ATP analog) or (B) ADP with the AAA+ domains and I domains shown for Rvb1 (pink and red, respectively) and Rvb2 (blue and orange, respectively) protomers.

(C) The different I-domain/I-domain conformation in the apo, ATP, and ADP states showing a rotation of 23° and 30° for the Apo and ADP states, respectively, compared with the apo position (dashed line).

(D) Side and top-down views of cryo-EM density docked with single Rvb1 and Rvb2 AAA+ domains in the respective upper and lower hexamers, showing a rotation of one ring relative to the other by 29° in the ATP state and 32° in ADP state compared with the apo-state position.

conformational changes that involve a stepwise shift of the I-domain/I-domain region around the dodecamer and a corresponding rotation of one hexamer ring relative to the other.

Refinement of the AAA+ Ring in the Dodecamer Identifies Higher-Resolution Nucleotide-Specific Features of the Apo, ATP, and ADP States

Given the large conformational changes we identify for the I-domain position, additional changes in the AAA+ ring that reflect nucleotide state remained a question. At increased density thresholds improved features were observed in the AAA+ domains, indicating that the hexamer rings are stable and that higher-resolution information may be present (Figure 2B). Therefore, we performed focused refinements of a single AAA+ ring for each of the dodecamer datasets (Figure S5A). The final maps from the apo-, ATP-, and ADP-state datasets are substantially improved (Figures 5A, 5B, S5B, and S5C) and show extensive regions of α-helical density and well-defined protomer subunits. The docked crystal structures fit in an arrangement similar to that of the dodecamer models, indicating that the conformations are consistent. Cross-correlation values of 0.89, 0.90, and 0.91 are obtained for the respective apo, ATP, and ADP states when the model and cryo-EM density maps are compared. Differences in density that correspond to the two protomers are identified, including density for the larger C-terminal helix in Rvb2, enabling their assignment in the map (Figure S5D). The increased resolution of the reconstructions enables the correct mirror symmetry to be determined unambiguously for the AAA+ rings and for the dodecamer reconstructions by comparison with the lower-resolution features (Figure S5E).

In the apo-state map distinct cavities are observed in both protomers that correspond to the empty nucleotide-binding pocket positioned between the Walker A and B motifs (Figure 5C and Movie S2). This cavity is not visible in the ATP- and ADP-state reconstructions and, instead, strong positive density is identified within the nucleotide pocket in ATP-apo and ADP-apo difference maps, indicating that nucleotide is present (Figure 5D). In the Rvb2 pocket of the ATP-state reconstruction the amount of positive density is modest, suggesting that the occupancy of

AMPPNP is likely lower. This is consistent with a lower ATP occupancy of Rvb2 compared with Rvb1 observed in the crystal structure of the ATP/apo complex (Lakomek et al., 2015). In the ADP-apo difference map, the substantial positive density observed in both protomers is likely attributable to the presence of nucleotide as well as conformational changes around the pocket, including the N-terminal helix that is known to become ordered when nucleotide is bound (Figure S5F). These focused reconstructions of the AAA+ ring establish the nucleotide states of the dodecamers and confirm nucleotide-dependent conformational changes surrounding the nucleotide-binding pocket that potentially direct the larger I-domain conformational changes and AAA+-ring rotation we have identified in the dodecamer.

DISCUSSION

Rvb1/2 is an essential AAA+ complex involved in the assembly and activity of numerous multimeric complexes, but how ATP binding and hydrolysis drive catalytic functions has been a major question. Here we have used cryo-EM to investigate the architecture and nucleotide-specific states of the dodecamer form of yeast Rvb1/2. By 2D classification we identified bent and straight conformations of the dodecamer characterized by different arrangements of the I domains that interact to join the hexamer rings together. These methods were crucial in identifying homogeneous, symmetric subpopulations that were further characterized by 3D classification and refinement. The resulting molecular models reveal distinct apo-, ATP-, and ADP-state conformations that involve movement of one AAA+ ring relative to the other while maintaining specific I-domain interactions that stabilize the dodecamer. While the hydrolysis mechanism by the highly conserved AAA+ domains of Rvb1/2 is well understood (Snider and Houry, 2008), how the I domains respond during the hydrolysis cycle to support substrate interactions has been a challenge to elucidate. Our reconstructions show that the conformation of the I domains and position of the hexamer rings are coordinated by the nucleotide state. Based on these results, we propose a model for the Rvb1/2 hydrolysis cycle where
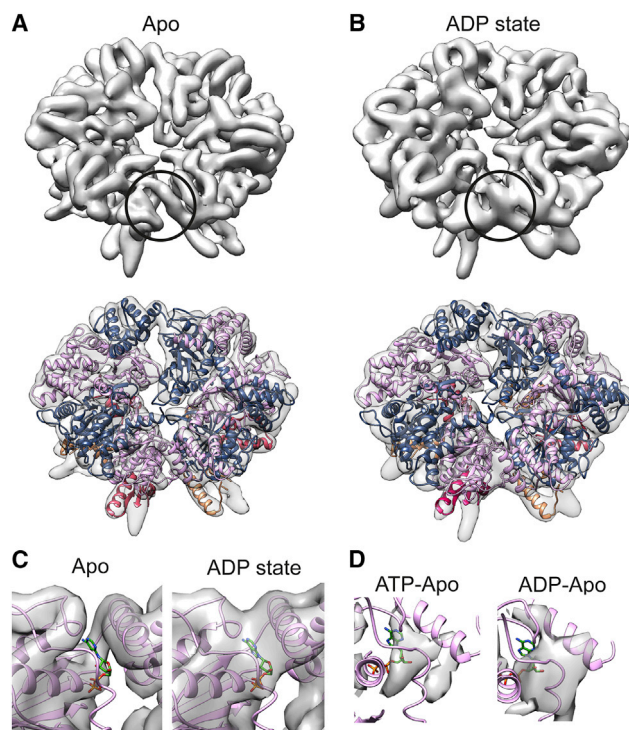
Figure 5. Focused Refinement of the AAA+ Hexamer Rings Identifies Higher-Resolution Nucleotide-Specific Differences

(A and B) Cryo-EM reconstructions and pseudo-atomic models (PDB: 4WW4) of the AAA+ hexamer ring from the (A) apo-state and (B) ADP-state dodecamer datasets showing higher-resolution features compared with full dodecamer map and approximate location of the nucleotide pocket for one protomer (circle).

(C) Expanded view of the Rvb1 nucleotide-binding pocket showing an empty pocket and nucleotide sitting outside the cryo-EM density for the apo state and a filled pocket with additional density surrounding the nucleotide for the ADP-state reconstruction.

(D) ATP-apo and ADP-apo difference maps at a threshold value above 6σ showing positive density (gray) in the Rvb1 nucleotide-binding pocket in the respective reconstructions.

Figure 6. Model for the ATP Hydrolysis-Driven Conformational Cycle of Rvb1/2

The Rvb1/2 dodecamer (gray), shown with highlighted Rvb1 (pink) and Rvb2 (blue) protomers, undergoes conformational changes upon ATP binding that involve a rotation of the globular I-domain tips that connect the hexamers together and a corresponding rotation of the AAA+ rings. Hydrolysis and formation of the ADP state drives additional modest rotations of the I domains and AAA+ ring. The conformational changes increase the offset between the protomers interacting across the dodecamer but do not change the overall dimensions or I-domain interaction interface. These changes together are proposed to regulate interactions between the I-domain region and DNA, RNA, or protein substrates, and provide mechanical force during helicase or remodeling functions.

the steps of ATP binding, hydrolysis, and nucleotide release trigger stepwise twists in the orientation of the I-domain globular tips and rotation of the AAA+ rings (Figure 6). These nucleotide-driven changes could alter DNA, RNA, or protein interactions mediated by the I domains and thus drive mechanical changes required for macromolecular assembly, remodeling, and helicase functions.

Nucleotide-dependent differences, including a minor tilting of the small and large AAA+ subdomains flanking the active site and the presence of the N-terminal strand over the nucleotide pocket, have been previously identified in nucleotide-bound protomers (Lakomek et al., 2015). Our reconstructions of the AAA+ rings identify nucleotide-specific differences that are consistent with these changes (Figures 5 and S5E), indicating that nucleotide binding alters the conformation of the AAA+ domains around the active site. In the primary sequence the I domain is inserted within the AAA+ domain, separating the Walker A and B motifs, so these changes around the nucleotide pocket likely propagate through the I domain to drive rotation of the distal α/β tip that
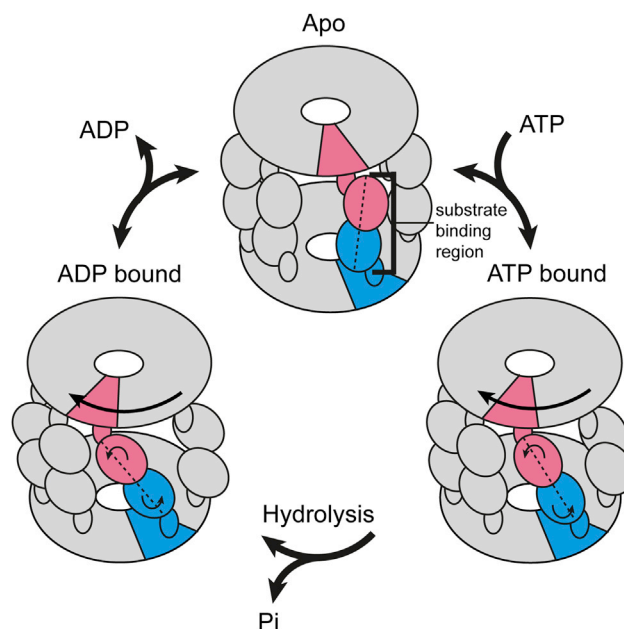
connects the hexamer rings in the dodecamer form. Based on the fits, the base region that connects the I domain to the AAA+ domain was unchanged in the different nucleotide states; therefore, the conformational changes appear to involve a rotation of the α/β tip region around the flexible β sheet that connects to the base (Figure S2H).

Our classification analysis uncovered distinct populations of "bent" dodecamers with different I-domain arrangements around the dodecamer (Figures 1B and S1E). In our 2D and 3D classification analysis (Figures S1D and S1E) we did not observe the alternating I-domain arrangement identified in recent structures of *C. thermophilum* Rvb1/2 (Lakomek et al., 2015; Silva-Martin et al., 2016), indicating that *S. cerevisiae* Rvb1/2 does not readily adopt this conformation under the solution-state conditions used for cryo-EM. The uniform Rvb1/2 I-domain arrangements we have characterized here are consistent with the findings of other structural studies (Cheung et al., 2010; López-Perrote et al., 2012; Matias et al., 2006). The asymmetric, bent conformations also show uniform I-domain density and thus appear to be stable and in distinct states, regardless of nucleotide state. Previous EM characterization identified compact and elongated dodecamers that agree with these dimensions (Jeganathan et al., 2015; López-Perrote et al., 2012). However, we find that for the straight configuration only minor

populations (<5%) are in these states, and the dodecamer primarily exists with an intermediate length of 140 Å. These distinct I-domain conformations we identify provide new insight into the flexibility of the dodecamer and may be functionally important for facilitating different modes of substrate interaction (Nano and Houry, 2013).

The apo conformation remained present in the ATP- and ADP-state data (Figure S4C and S4D). This could be attributed to partial nucleotide occupancy or the flexibility of the I domains remaining a significant factor, and these states readily interchange. It is also possible that ATP binding and hydrolysis may not occur in all protomers at once to drive the conformational changes in a concerted mechanism, but instead occur independently or sequentially during substrate remodeling events. We determined that our dodecamer sample was active for ATP hydrolysis and equivalent to those in other published studies (Gribun et al., 2008). Furthermore, by performing a 3D classification using the ADP state as a starting model we determined that this conformation was not detectable in the apo data (Figure S4G), confirming that it requires nucleotide binding. Thus, the dodecamer population is responsive to nucleotide, and the apo and nucleotide-bound conformations appear to exist in equilibrium.

Cryo-EM and mass spectrometry analysis of the INO80 complex place the Rvb1/2 dodecamer in the head region of the complex, interacting with the Snf2 ATPase and RecA2 domains of INO80 and flanking the nucleosome (Tosi et al., 2013). In other work Rvb1/2 is reported to exist as a hexamer in INO80 and SWR1 complexes (Nguyen et al., 2013; Watanabe et al., 2015), functioning as an interaction platform for key catalytic components of the complexes. Based on our results, nucleotide-dependent conformational changes are expected to occur in the hexamer form as well, although the specific arrangement of I domains could be different compared with the dodecamer. While additional work is necessary to characterize the hexamer/dodecamer state of Rvb1/2 in these complexes, the nucleotide-dependent conformational changes we identify are likely important for regulating these scaffolding interactions. Indeed, the presence of ATP, but not Rvb1/2 ATPase activity, was required for Arp5 recruitment and INO80 activity, leading to the conclusion that the ATP conformation of Rvb1/2 is important for interactions with INO80 (Jónsson et al., 2004). Thus, the nucleotide-bound conformation of the I domains could be important for stabilizing the active state of chromatin remodeling complexes while hydrolysis and ADP release may function in disassembly. The presence of ATP has also been shown to alter Rvb1/2 interactions with box C/D snoRNP subunits, enhance binding to 15.5K and BCD1, and cause the release of Nop17 and Tah1/Pih1 (Kakihara et al., 2014; McKeegan et al., 2009; Prieto et al., 2015). The nucleotide-dependent conformational changes we identify together with these studies support a functional role for ATP binding and hydrolysis by Rvb1/2 in driving mechanical changes via I-domain interactions during macromolecular remodeling events.

Based on the established helicase activity of Rvb1/2 (Gribun et al., 2008) and known homologies to bacterial RuvB (Makino et al., 1999), a compelling function of these conformational changes is to drive DNA/RNA unwinding events by providing mechanical force that alters direct interactions with the I domains. However, additional studies are needed to establish helicase functions of Rvb1/2 in the context of its position in larger complexes. In summary, our work has provided important insight into the architecture and I-domain flexibility of the Rvb1/2 dodecamer, revealing specific apo, ATP, and ADP conformations that likely direct catalytic functions in the assembly and activity of large macromolecular machines. Additional work will help elucidate the role of this conformational cycle in the many cellular pathways that are dependent on the Rvb1/2 complex.

EXPERIMENTAL PROCEDURES

Purification, Size-Exclusion Chromatography, and ATP Hydrolysis Analysis of Rvb1/2

See Supplemental Experimental Procedures.

EM Sample Preparation and Data Collection

Untagged wt Rvb1/2 dodecamer, or mutant complexes were buffer-exchanged into 25 mM HEPES, 150 mM KCl, and 6 mM β-mercaptoethanol. For nucleotide binding, samples were incubated in 5 mM MgCl$_2$ and 200 μM AMPPNP or ADP (Sigma) for 30 min. Negative staining was performed as described by Ohi et al. (2004) and imaged on a T12 (FEI) at 1–2 μm defocus, and recorded using a 4k × 4k CCD camera (Gatan). For cryo-EM, samples were diluted to 0.3 mg/ml and applied to holey-carbon (Quantifoil) grids. Vitrification was performed using a Vitrobot (FEI). Data were collected using a Titan Krios (FEI) equipped with a K2 Summit Direct Detection camera (Gatan), and operated at 300 kV with nominal 50,000× magnification, with a pixel size of 1 Å/pixel in counted mode. Images were recorded with a 1.8–3 μm defocus. A 6-s exposure time was taken in 30 subframes with a ~5 e⁻/pixel/s dose, giving 1 e⁻/pixel per subframe and an accumulated dose of 30 e⁻/pixel. Subframes were drift corrected and summed using driftcorr (Li et al., 2013).

Cryo-EM Data Processing

Particles were selected using BOXER in EMAN2 (Ludtke et al., 1999). Total datasets included 3,800 micrographs with 241,658 particles for the apo dataset, 1,600 micrographs with 103,639 selected particles for the ATP state, and 3,303 micrographs with 217,746 selected particles for the ADP state. Defocus values were estimated using CTFFIND3 (Mindell and Grigorieff, 2003). 2D and 3D processing was performed using RELION (Scheres, 2012). Particles from the bent and heterogeneous class averages were removed prior to 3D processing. To improve the angular distribution we included all top-view particles as well as tilted-view particles with parallel AAA rings, determined by 2D classification. A 3D cylinder was used as a starting model for refinement (Figure S2A). 3D classification with four classes was performed with 4 Å/pixel particle images and D6 symmetry imposed, due to the known low-resolution pseudo-symmetry, for 25 iterations. Two similar classes (1 and 3) were combined for 13 rounds of refinement. Refinement of individual classes was performed but resulted in lower-resolution final models (data not shown). Remaining classes were poorly resolved (class 2) or elongated due to the presence of bent particles (class 4), identified by additional 2D classification, and not included. D3 symmetry was imposed during the higher-resolution refinement because of the established 1–2 alternating subunit organization with 2 Å/pixel particle images. The angular distribution for the apo dodecamer reconstruction is shown in Figure S2D; particle distributions were similar for all other reconstructions. For the asymmetric reconstructions (Figure S1F), particles from the bent 2D classes were pooled for 3D classification using a low-pass-filtered apo reconstruction as the initial model. For the ATP and ADP final models a single, well-defined 3D class was chosen for refinement and D6 symmetry was imposed for 14 and 17 rounds of refinement, respectively (Figures S4C and S4D). D3 symmetry showed no improvement (data not shown). To test for model bias and establish the nucleotide specificity, we also performed refinements of the ATP and ADP data using a 20 Å low-pass-filtered apo-state starting model and a classification with the whole apo dataset using an ADP starting model (Figures S4E and S4F). The final models were generated from 66,597, 13,630, and 34,173 particles for the apo, ATP, and ADP states, respectively, with indicated resolutions of 8.3, 9.5, and 7.8 Å using the gold-standard FSC = 0.143 criterion and 9.4, 11.6, and 9.8 Å at FSC = 0.5.

For the focused refinement, a mask was created from an apo model that incorporated one AAA+ ring and I-domain bases (Figure S5A) with C6 symmetry imposed and a "soft" Gaussian edge. This mask was applied for 21, 17, and 20 rounds of refinement for the apo, ATP, and ADP refinements, respectively, using the data that went into the dodecamer reconstructions, with C3 symmetry imposed. RELION was used for post-processing, using auto-masking and b factors of −250, −300, and −150 for the apo-, ATP-, and ADP-state AAA+ maps, respectively. The indicated resolutions of the final apo-, ATP-, and ADP-state models of the AAA+ hexamers were 6.4, 8.3, and 7.1 Å, respectively. The accession codes for the final maps, deposited in the Electron Microscopy DataBank, are EMD-3080 (apo dodecamer), EMD-3081 (ATP dodecamer), EMD-3082 (ADP dodecamer), EMD-3083 (apo focused), EMD-3084 (ATP focused), and EMD-3085 (ADP focused).

Model Fitting and Visualization

Pseudo-atomic models were achieved using UCSF Chimera (Pettersen et al., 2004) and Situs (Wriggers, 2010), using the collage function for the simultaneous docking of multiple fragments. The full-length Rvb1/2 crystal structure bound to ATP/apo (PDB: 4WVY) or in the ADP state (PDB: 4WW4) was used due to the completeness of the structures (Lakomek et al., 2015). The Rvb1 and two AAA+ domains (residues 11–121 and 297–449 of Rvb1; 26–127 and 292–448 of Rvb2), the I-domain base with extended β sheet (Rvb1 122–134, 229–296; Rvb2 128–137, 232–291) or without (Rvb1 238–296; Rvb2 240–291), and the globular tip (Rvb1 135–228; Rvb2 138–231) were docked as rigid bodies for each protomer. Flexible loops within the I-domain bases were also removed to aid fitting (Rvb1 250–274; Rvb2 249-269). The degree of rotation for the conformational changes was determined by aligning one AAA+ ring in the dodecamer and measuring the angles about the rotation-symmetry axis between corresponding regions on the I domains or second AAA rings. The correct mirror symmetry was confirmed by the fits of the AAA+ rings of the apo- and ADP-state focused reconstructions. UCSF Chimera was used for visualization, segmenting the maps, and cross-correlation analysis of the models.

SUPPLEMENTAL INFORMATION

Supplemental Information includes Supplemental Experimental Procedures, five figures, and two movies and can be found with this article online at http://dx.doi.org/10.1016/j.str.2016.03.018.

AUTHOR CONTRIBUTIONS

C.A.E. helped design the study and performed the experiments and analysis, and drafted the manuscript; M.S. performed experiments and analyzed cryo-EM data; L.Z. performed initial experiments; N.N. performed ATPase assays; W.A.H. participated in experimental design and data analysis, and edited the manuscript; D.R.S. designed and supervised the study and edited the manuscript.

REFERENCES

Cheung, K.L.Y., Huen, J., Kakihara, Y., Houry, W.A., and Ortega, J. (2010). Alternative oligomeric states of the yeast Rvb1/Rvb2 complex induced by histidine tags. J. Mol. Biol. *404*, 478–492.

Gerhold, C.B., and Gasser, S.M. (2014). INO80 and SWR complexes: relating structure to function in chromatin remodeling. Trends Cell Biol. *24*, 619–631.

Gorynia, S., Bandeiras, T.M., Pinho, F.G., McVey, C.E., Vonrhein, C., Round, A., Svergun, D.I., Donner, P., Matias, P.M., and Carrondo, M.A. (2011). Structural and functional insights into a dodecameric molecular machine—the RuvBL1/RuvBL2 complex. J. Struct. Biol. *176*, 279–291.

Gribun, A., Cheung, K.L.Y., Huen, J., Ortega, J., and Houry, W.A. (2008). Yeast Rvb1 and Rvb2 are ATP-dependent DNA helicases that Form a heterohexameric complex. J. Mol. Biol. *376*, 1320–1333.

Izumi, N., Yamashita, A., Iwamatsu, A., Kurata, R., Nakamura, H., Saari, B., Hirano, H., Anderson, P., and Ohno, S. (2010). AAA+ proteins RUVBL1 and RUVBL2 coordinate PIKK activity and function in nonsense-mediated mRNA decay. Sci. Signal. *3*, ra27.

Jeganathan, A., Leong, V., Zhao, L., Huen, J., Nano, N., Houry, W.A., and Ortega, J. (2015). Yeast Rvb1 and Rvb2 proteins oligomerize as a conformationally variable dodecamer with low frequency. J. Mol. Biol. *427*, 1875–1886.

Jónsson, Z.O., Dhar, S.K., Narlikar, G.J., Auty, R., Wagle, N., Pellman, D., Pratt, R.E., Kingston, R., and Dutta, A. (2001). Rvb1p and Rvb2p are essential components of a chromatin remodeling complex that regulates transcription of over 5% of yeast genes. J. Biol. Chem. *276*, 16279–16288.

Jónsson, Z.O., Jha, S., Wohlschlegel, J.A., and Dutta, A. (2004). Rvb1p/Rvb2p recruit Arp5p and assemble a functional Ino80 chromatin remodeling complex. Mol. Cell *16*, 465–477.

Kakihara, Y., Makhnevych, T., Zhao, L., Tang, W., and Houry, W.A. (2014). Nutritional status modulates box C/D snoRNP biogenesis by regulated subcellular relocalization of the R2TP complex. Genome Biol. *15*, 404.

Kanemaki, M., Kurokawa, Y., Matsu-ura, T., Makino, Y., Masani, A., Okazaki, K., Morishita, T., and Tamura, T.A. (1999). TIP49b, a new RuvB-like DNA helicase, is included in a complex together with another RuvB-like DNA helicase, TIP49a. J. Biol. Chem. *274*, 22437–22444.

Lakomek, K., Stoehr, G., Tosi, A., Schmailzl, M., and Hopfner, K.-P. (2015). Structural basis for dodecameric assembly states and conformational plasticity of the full-length AAA+ ATPases Rvb1·Rvb2. Structure *23*, 483–495.

Li, X., Mooney, P., Zheng, S., Booth, C.R., Braunfeld, M.B., Gubbens, S., Agard, D.A., and Cheng, Y. (2013). Electron counting and beam-induced motion correction enable near-atomic-resolution single-particle cryo-EM. Nat. Methods *10*, 584–590.

López-Perrote, A., Muñoz-Hernández, H., Gil, D., and Llorca, O. (2012). Conformational transitions regulate the exposure of a DNA-binding domain in the RuvBL1-RuvBL2 complex. Nucleic Acids Res. *40*, 11086–11099.

Ludtke, S.J., Baldwin, P.R., and Chiu, W. (1999). EMAN: semiautomated software for high-resolution single-particle reconstructions. J. Struct. Biol. *128*, 82–97.

Makino, Y., Kanemaki, M., Kurokawa, Y., Koji, T., and Tamura, T. (1999). A rat RuvB-like protein, TIP49a, is a germ cell-enriched novel DNA helicase. J. Biol. Chem. *274*, 15329–15335.

Matias, P.M., Gorynia, S., Donner, P., and Carrondo, M.A. (2006). Crystal structure of the human AAA+ protein RuvBL1. J. Biol. Chem. *281*, 38918–38929.

Matias, P.M., Baek, S.H., Bandeiras, T.M., Dutta, A., Houry, W.A., Llorca, O., and Rosenbaum, J. (2015). The AAA+ proteins Pontin and Reptin enter adult age: from understanding their basic biology to the identification of selective inhibitors. Front Mol. Biosci. *2*, 17.

McKeegan, K.S., Debieux, C.M., and Watkins, N.J. (2009). Evidence that the AAA+ proteins TIP48 and TIP49 bridge interactions between 15.5K and the related NOP56 and NOP58 proteins during box C/D snoRNP biogenesis. Mol. Cell Biol. *29*, 4971–4981.

Mindell, J.A., and Grigorieff, N. (2003). Accurate determination of local defocus and specimen tilt in electron microscopy. J. Struct. Biol. *142*, 334–347.

Nano, N., and Houry, W.A. (2013). Chaperone-like activity of the AAA+ proteins Rvb1 and Rvb2 in the assembly of various complexes. Philos. Trans. R. Soc. Lond. B Biol. Sci. *368*, 20110399.

Neuwald, A.F., Aravind, L., Spouge, J.L., and Koonin, E.V. (1999). AAA+: a class of chaperone-like ATPases associated with the assembly, operation, and disassembly of protein complexes. Genome Res. *9*, 27–43.

Nguyen, V.Q., Ranjan, A., Stengel, F., Wei, D., Aebersold, R., Wu, C., and Leschziner, A.E. (2013). Molecular architecture of the ATP-dependent chromatin-remodeling complex SWR1. Cell *154*, 1220–1231.

Ohi, M., Li, Y., Cheng, Y., and Walz, T. (2004). Negative staining and image classification—powerful tools in modern electron microscopy. Biol. Proced. Online *6*, 23–34.

Pettersen, E.F., Goddard, T.D., Huang, C.C., Couch, G.S., Greenblatt, D.M., Meng, E.C., and Ferrin, T.E. (2004). UCSF Chimera–a visualization system for exploratory research and analysis. J. Comput. Chem. *25*, 1605–1612.

Prieto, M.B., Georg, R.C., Gonzales-Zubiate, F.A., Luz, J.S., and Oliveira, C.C. (2015). Nop17 is a key R2TP factor for the assembly and maturation of box C/D snoRNP complex. BMC Mol. Biol. *16*, 7.

Scheres, S.H.W. (2012). RELION: implementation of a Bayesian approach to cryo-EM structure determination. J. Struct. Biol. *180*, 519–530.

Shen, X., Mizuguchi, G., Hamiche, A., and Wu, C. (2000). A chromatin remodelling complex involved in transcription and DNA processing. Nature *406*, 541–544.

Silva-Martin, N., Dauden, M.I., Glatt, S., Hoffmann, N.A., Kastritis, P., Bork, P., Beck, M., and Muller, C.W. (2016). The combination of x-ray crystallography and cryo-electron microscopy provides insight into the overall architecture of the dodecameric Rvb1/Rvb2 complex. PLoS One *11*, e0146457.

Snider, J., and Houry, W.A. (2008). AAA+ proteins: diversity in function, similarity in structure. Biochem. Soc. Trans. *36*, 72–77.

Torreira, E., Jha, S., López-Blanco, J.R., Arias-Palomo, E., Chacón, P., Cañas, C., Ayora, S., Dutta, A., and Llorca, O. (2008). Architecture of the pontin/reptin complex, essential in the assembly of several macromolecular complexes. Structure *16*, 1511–1520.

Tosi, A., Haas, C., Herzog, F., Gilmozzi, A., Berninghausen, O., Ungewickell, C., Gerhold, C.B., Lakomek, K., Aebersold, R., Beckmann, R., et al. (2013). Structure and subunit topology of the INO80 chromatin remodeler and its nucleosome complex. Cell *154*, 1207–1219.

Tucker, P.A., and Sallai, L. (2007). The AAA+ superfamily—a myriad of motions. Curr. Opin. Struct. Biol. *17*, 641–652.

Venteicher, A.S., Meng, Z., Mason, P.J., Veenstra, T.D., and Artandi, S.E. (2008). Identification of ATPases pontin and reptin as telomerase components essential for holoenzyme assembly. Cell *132*, 945–957.

Watanabe, S., Tan, D., Lakshminarasimhan, M., Washburn, M.P., Erica Hong, E.-J., Walz, T., and Peterson, C.L. (2015). Structural analyses of the chromatin remodelling enzymes INO80-C and SWR-C. Nat. Commun. *6*, 7108.

Wriggers, W. (2010). Using Situs for the integration of multi-resolution structures. Biophysical Rev. *2*, 21–27.

Wu, W.H., Alami, S., Luk, E., Wu, C.H., Sen, S., Mizuguchi, G., Wei, D., and Wu, C. (2005). Swc2 is a widely conserved H2AZ-binding module essential for ATP-dependent histone exchange. Nat. Struct. Mol. Biol. *12*, 1064–1071.

Yao, W., Beckwith, S.L., Zheng, T., Young, T., Dinh, V.T., Ranjan, A., and Morrison, A.J. (2015). Assembly of the Arp5 subunit involved in distinct INO80 chromatin-remodeling activities. J. Biol. Chem. *290*, 25700–25709.

Zaarur, N., Xu, X., Lestienne, P., Meriin, A.B., McComb, M., Costello, C.E., Newnam, G.P., Ganti, R., Romanova, N.V., Shanmugasundaram, M., et al. (2015). RuvbL1 and RuvbL2 enhance aggresome formation and disaggregate amyloid fibrils. EMBO J. *34*, 2363–2382.

Zhao, R., Davey, M., Hsu, Y.-C., Kaplanek, P., Tong, A., Parsons, A.B., Krogan, N., Cagney, G., Mai, D., Greenblatt, J., et al. (2005). Navigating the chaperone network: an integrative map of physical and genetic interactions mediated by the hsp90 chaperone. Cell *120*, 715–727.